Room-Temperature Bistability in Spin Crossover-Loaded Metal–Organic Frameworks

Yuwei Shen, Johanna Woodburn, Soraya Bouras, Shan Dai, Iurii Dovgaliuk, Jean-Marc Grenèche, Gilles Patriarche, Latévi Max Lawson Daku, Christian Serre, Antoine Tissot

Room Temperature bistability in spin crossover loaded Metal-Organic Frameworks

Yuwei Shen,[1] Johanna Woodburn,[1] Soraya Bouras,[1] Shan Dai,[1] Iurii Dovgaliuk,[1] Jean-Marc Grenèche,[2] Gilles Patriarche,[3] Latévi Max Lawson Daku,[4] Christian Serre,*[1] Antoine Tissot*[1]

[1] *Institut des Matériaux Poreux de Paris, Ecole Normale Supérieure, ESPCI Paris, CNRS, PSL University, 75005 Paris, France*
[2] *Institut des Molécules et Matériaux du Mans -IMMM-UMR CNRS 6283, Le Mans Université, 72085, Le Mans, Cedex 9, France*
[3] *Université Paris-Saclay, CNRS, Centre de Nanosciences et de Nanotechnologies, 91120 Palaiseau, France*
[4] *Department of Physical Chemistry, University of Geneva, 1211 Geneva, Switzerland*

e-mail addresses: christian.serre@ens.psl.eu; antoine.tissot@ens.psl.eu

Abstract
In this article, we present an unprecedented strategy to prepare bistable porous nanocrystals based on the anchoring of switchable molecules in the pores of a host matrix through strong host-guest interactions. More precisely, we have inserted a prototypical Fe(III) spin crossover complex in MOF-808, a chemically robust large pores Zr-based MOF. The loaded nanocrystals present an hysteretic thermal spin transition close to room temperature that is independent of the complex loading and the MOF particle size while remaining highly porous, which opens up opportunities for their use as chemical sensors.

Introduction

Bistable nano-objects are particularly appealing for several applications such as data storage, display devices and sensing.[1,2] Spin crossover (SCO) compounds are typically d^4 to d^7 metal complexes in octahedral geometries that can undergo a conversion between a low spin (LS) and a high spin (HS) state upon various *stimuli* including temperature, pressure, light or a change in chemical environment.[3] In some cases, the LS and HS states can be stable in a given temperature range, making them prototypical bistable objects. Bistability is generally related to the volume change of the SCO species that occurs upon the LS-HS spin transition, due to the population of antibonding orbitals of the spin crossover cation. Indeed, in the crystalline state, this volume change can affect both neighboring spin crossover entities through short-range interactions and the whole solid through so-called elastic interactions.[4,5] Therefore, a common strategy for the synthesis of bistable spin crossover solids relies on the design of solids with strong intermolecular interactions. In the case of molecular complexes, this can be achieved by using linkers that can interact with each other, such as through π-stacking or H-bonding.[3,6] However, the scope of design that can be reached is often limited as it is difficult to predict and control how species will be packed in a molecular crystal. This limitation can be overcome by the design of coordination frameworks where the spin

crossover centers are linked by coordination bonds, resulting in 1 to 3D compounds with bistability at room temperature.[3] In addition, some of these materials are porous, opening up opportunities for the preparation of host-guest switchable compounds.[7–9]

In most cases, the bistability is related to the crystal size and often disappears at the nanoscale.[10,11] Indeed, reducing the crystal size domain decreases the strength of the elastic interactions that often drive cooperativity. Thus, the preparation of bistable spin crossover nanocrystals is still challenging, although a prerequisite for their integration into electronic devices. It is therefore of particular interest to develop (nano)materials where the switching behavior does not depend on elastic interactions. Ideally, one could tailor strong short-range interactions between the spin crossover center and its surrounding. This concept has previously been evidenced at the macroscopic scale, where the cooperative character of the thermal spin transition of spin crossover micro- or nano-crystals is tuned by dispersing them in different media.[12–15] Alternatively, at the nanoscale, loading molecular complexes into ordered nanoporous materials could lead to similar effects. Several reports have described the loading of spin crossover complexes into layered solids, zeolites or Metal-Organic Frameworks (MOFs).[16–20] Diamagnetic MOFs are particularly appealing for such application, due to their highly tunable, ordered porous structure whose functions can easily be adapted to the targeted application.[21,2] For example, some of us have encapsulated the $Fe^{III}(sal_2trien)^+$ spin crossover cation in the mesoporous MIL-100(Al) by *in situ* synthesis of the complex in the MOF' pores, giving rise to a compound presenting a spin crossover upon water sorption at room temperature.[22] Recently, we also anchored $[Fe^{II}(BPI)(HBPI)(ClO_4)_2]^-$ in MFU-4(l) and MIL-100(Al) by the sequential installation of the linkers and Fe(II) cations to obtain solids with a solvatochromic behavior upon sorption of alcohols.[23] However, to date, none of these materials exhibit abrupt thermal spin transitions with the opening of an hysteresis loop.[22–24] Here, we describe the loading of a prototypical Fe(III) spin crossover complex in MOF-808, a chemically robust large pores (~18 Å) Zr-based MOF.[25] The solids present an hysteretic thermal spin transition close to room temperature that is independent of the SCO complex loading and the MOF particle size while remaining highly porous, which opens up opportunities for their use as chemical sensors.

Experimental section

All commercial available chemicals were used without further purification.

Synthesis of MOF-808 nanocrystals

- *120 nm MOF-808***.** This synthesis was adapted from the procedure described by H. Furukawa et al.:[25] 1.49 g 1,3,5-benzentricarboxylic acid and 2.16 g $ZrOCl_2 \cdot 8H_2O$ were subsequently dissolved to a mixture of 128mL DMF and 133 mL formic acid in a 500 mL screw-capped glass jar. The solution was heated at 110 °C for 48 h. The white powder was collected and then refluxed in 250 mL DMF at 100 °C and 250 mL acetone at 60 °C, respectively. The final product was filtrated and dried in a vacuum oven.
- *30 nm MOF-808.* The room-temperature synthesis of MOF-808 was previously reported by S. Dai et al.:[26] Zr_6 oxoclusters were firstly synthesized by mixing 200g of $ZrCl_4$ with 300 mL acetic acid and 500 mL isopropanol at 120 °C for 1 hour. Then 1.2 g of Zr_6 oxoclusters was dispersed in 1 mL formic acid, followed by the addition of 1.67 ml of H_2O. Subsequently, 300 mg 1,3,5-benzentricarboxylic acid was added and the reaction was stirred

at room temperature overnight. The product was washed with H_2O and EtOH, respectively, and dried under a vacuum.

- *850 nm MOF-808*. A similar procedure was performed using different amounts of all starting materials: 0.6 g Zr_6 oxoclusters, 3 mL formic acid, 5 ml H_2O, and 150 mg 1,3,5-benzentricarboxylic acid.

Synthesis of Fe(sal$_2$trien)NO$_3$ (1)

This synthesis was adapted from the procedure described by Pritchard et al.:[27] 855 mg of salicylaldehyde and 500 mg of triethylenetetramine were added to 30 mL of MeOH under stirring. It was later mixed with another solution of 100 mg of NaOH in 30 mL of MeOH. Subsequently, 1.41 g of $Fe(NO_3).9H_2O$ was dissolved in 10 mL of MeOH and then added to the previous solution. After 2h under stirring at room temperature, the solvent was evaporated under reduced pressure. The remaining solid were recrystallized in water. Dark violet crystals were collected through filtration and dried under vacuum.

Synthesis of 1⊂MOF-808

For a typical synthesis of **1⊂MOF-808**, 100 mg MOF-808 was immersed in a solution containing 50 mg Fe(sal$_2$trien)NO$_3$ in 25mL of dichloromethane and stirred for 2h at room temperature. The sample was then collected by centrifugation, washed three times with 30 ml dichloromethane, and dried in a vacuum oven. The loading amount of **1** was controlled by changing the MOF-808/**1** ratio and the reaction time (see Supporting information for the detailed procedure).

Methods:

- Laboratory powder X-ray diffraction (PXRD): The conventional powder X-ray diffraction data were measured at room temperature with a Bruker D8 Advance diffractometer in Debye-Scherrer geometry (transmission mode), in 2-40° 2θ range, equipped with Cu Kα radiation (λ = 1.5406 Å).
- Synchrotron powder X-ray diffraction (SPXRD) and pair distribution function analysis (PDF): The high energy (λ = 0.5130 Å) SPXRD data were collected at CRISTAL beamline (SOLEIL, France). The samples were loaded to 1 mm glass capillaries and measured at room temperature using 2 circle diffractometer with 1D detector (Mythen). Prior the transformation of powder diffraction pattern to PDF spectra, the empty glass 1.0 mm capillary was measured as a reference for the background subtraction. The data reduction was performed using PDFgetX3 software.[28] The differential PDF was obtained after subtraction of the normalized Zr-Zr correlation (3.5 Å) from the Fe(sal$_2$trien)NO$_3$-loaded and empty MOF-808, respectively. The calculated PDF of Fe(sal$_2$trien)$^+$ was obtained using PDFgui software[29] from one of the crystal structures of Fe(sal$_2$trien)$^+$ salts[30], taking into account only the correlations of Fe(sal$_2$trien)$^+$.
- Thermogravimetric analysis (TGA): TGA measurements were performed on Mettler Toledo TGA/DSC 1, STAR®System apparatus under N_2 atmosphere at a heating rate of 5 °C.min^{-1} up to 600 °C.
- Raman spectroscopy: Raman spectra were collected using an Anton Paar Cora 7200 spectrometer equipped with a 785 nm excitation Laser, a fiber optics based probe and a CCD detector controlled by the Cora7000, V2.2.0 software.
- Infrared spectroscopy: Infrared spectra were measured with a Nicolet iS5 FTIR ThermoFisher spectrometer.
- N_2 porosimetry: N_2 sorption measurements were performed at 77 K on the Micromeretics Triflex apparatus. The MOF-808 samples (ca. 40 mg) were activated by

heating the powder at 180 °C under a secondary vacuum for 12h. For the 1⊂MOF-808 samples, the activation was performed at 120 °C.

- SEM-EDX: Scanning Electron Microscopy coupled with energy-dispersive X-ray spectroscopy (SEM-EDX) results were recorded with FEI Magellan 400 scanning electron microscope. Average Fe and Zr values (Fe atm% to Zr) were calculated based on taking several points for each sample.
- High-resolution transmission electron microscopy: High-resolution TEM images (HRTEM) were acquired on a Titan Themis 200 microscope operating at 200 kV. This microscope is equipped with a Ceta 16M hybrid camera from Thermo Fischer Scientific capable of working under low electron irradiation conditions. The HRTEM images are obtained in low dose conditions with an irradiation current between 100 and 250 electrons per square angstroms. For the TEM grid preparation, a 2 µl drop of the solution is placed on a 200 mesh copper grid covered with a pure carbon membrane (from Ted Pella).
- Magnetic measurements: Magnetic measurements were carried out with a Quantum Design SQUID Magnetometer with an applied field of 5 kOe. Samples of *ca*. 10 mg were enclosed in a diamagnetic sample holder. The samples were heated in the magnetometer for 10 minutes at 400 K prior to any measurement to remove the traces of solvent in the MOF pores. The magnetic measurements have been processed as follows: In a first state, the magnetization has been corrected from the diamagnetic contribution of both the sample holder and the host diamagnetic MOF. This correction was performed empirically in order to get an MT product that remains constant at low temperatures (below 200 K). Then, the magnetization has been normalized by the magnetic field and the mass of the compound used. This normalization leads to a magnetic susceptibility expressed by the unit of mass. Further normalization in order to get the magnetic susceptibility by mole of Iron complex has been performed using the Zr/Fe atomic ratio obtained by EDX and knowing the molar weight of both the host MOF and the encapsulated complex. Note that due to the number of hypotheses involved during the data processing (diamagnetic correction, amount of complex loaded in the MOF...), the final $\chi_M T$ product is obtained with a precision of *ca*. 0.3 emu.K.mol^{-1}.
- Mössbauer spectrometry: The experiments were carried out in transmission geometry using a 925 MBq γ-source of ^{57}Co/Rh mounted on a conventional constant acceleration driving unit. Sample 1⊂MOF-808 was enriched in ^{57}Fe to have a Mössbauer sample consisting of a thin and homogeneous layer of powder containing 5 mg Fe/cm^2 in order to have a reasonable registration time (i.e. about 10h) and to avoid thickness effects. The Mössbauer spectra were obtained at 300K and 77K using a bath cryostat and then fitted using the MOSFiT program (F. Varret and J. Teillet, unpublished MOSFiT program, Université Le Mans, France) involving quadrupolar components composed of Lorentzian lines. The source velocity scale was calibrated using α-Fe as a standard at RT, while the values of isomer shift refer to that of α-Fe at RT. The quadrupolar components show some asymmetry which is due to the presence of preferential orientation that was verified on a spectrum recorded with the magic angle configuration.[31,32]

Results and discussion

- **Synthesis of Fe^{III}(sal$_2$trien)⊂MOF-808 hybrid solids**

MOF-808 or $Zr_6O_4(OH)_4(BTC)_2(HCOO)_6$ is a chemically robust nanoporous Zr(IV)-based MOF composed of 6-connected Zr_6 nodes and trimesic acid (or 1,3,5 Benzenetricarboxylic acid). The framework, with a *spn* topology, consists of 4.8 Å tetrahedral cages and large

adamantane cages with a free diameter of 18.4 Å and exhibits a BET surface area close to 2,000 $m^2.g^{-1}$ (N_2 porosimetry at 77K).[25] Recently, some of us have reported a scalable green room temperature synthesis, giving access to a control of the MOF particle size from 30 to 850 nm,[26] which was first applied to the catalytic hydrolysis of peptide bonds.[33] Given the large pore size and good chemical stability of MOF-808, along with its colorless and diamagnetic nature, we selected this MOF as a host matrix to encapsulate SCO complexes towards a comprehensive investigation of the confinement effect. $Fe^{III}(sal_2trien)NO_3$ (noted **1**) was loaded into MOF-808 with three different particle sizes prepared either through the room temperature approach (30 nm, 850 nm) or using solvothermal conditions (120 nm) by soaking the MOF in a concentrated solution of Fe(III) complex in dichloromethane at room temperature. The molecular size of $Fe^{III}(sal_2trien)^+$ is approximately 8 Å, which is by far small enough to enter the adamantane pores of MOF-808. Excess SCO complexes were removed by repeated washing of the solids with dichloromethane (details in supporting information). Despite the fact that the windows of MOF-808 pores are larger than the size of $Fe^{III}(sal_2trien)^+$ cations, negligible leakage of SCO complexes was observed after additional washings using the same solvent. This suggests the presence of strong host-guest interactions between the MOF matrix and the inserted complexes.

The color of the solid turned from colorless to black-brown after loading, in agreement with the successful encapsulation of the SCO complex. PXRD patterns of **1**⊂MOF-808 confirmed that the structural integrity of the host matrix was preserved after the loading process (**Fig. 1a and Fig. S1)**. As expected, the relative intensity of the low-angle peaks was reduced in $Fe^{III}(sal_2trien)$⊂MOF-808 compared to MOF-808, further demonstrating the successful loading of the SCO complex in the pores of the MOF rather than complex recrystallization or anchoring to the MOF surface.[34] HRTEM further proved that the MOF crystals maintained their high crystallinity after loading, with well-defined polyhedral shapes, even for the smallest nanocrystals (**Fig. 1b-c and Fig. S2**). In addition, the STEM-EDX elemental mappings (**Fig. 1d and Fig. S3**) revealed a regular distribution of SCO complexes in MOF-808 nanocrystals. Energy dispersive X-ray (EDX) analysis revealed the average Fe : Zr atomic ratio of 0.21 for a saturated loading in 120 nm MOF-808 particle (sample denoted as 1⊂120 nm-21%), corresponding to 5.1 complex molecules per host cage, in good agreement with thermogravimetric analysis (**Fig. S4)**. Since the volume of a single $Fe(sal_2trien)NO_3$ complex is around 540 $Å^3$ according to the single crystal structure of the complex, a theoretical maximal loading capacity of 8 complexes per adamantane cage was estimated, in good agreement with the SEM-EDX and STEM-EDX results (**Fig. S5**). The iron content of the samples with different particle sizes and complex loading is presented in **Table 1**.

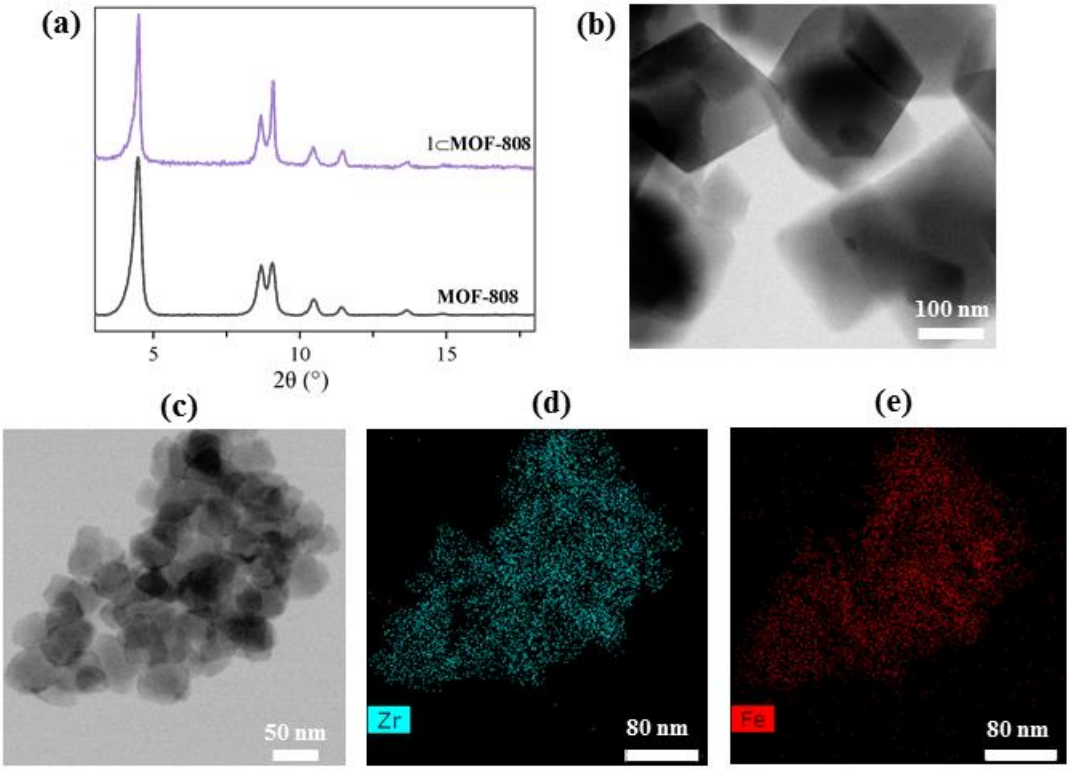

Figure 1. a) Powder X-Ray Diffraction pattern (λ_{Cu} = 1.5406 Å) of 120 nm MOF-808 and Fe(sal$_2$trien)⊂MOF-808 nanocrystals; b-c) Bright Field STEM images of 120 nm and 30 nm MOF-808 particles*;* d-e) STEM-EDX elemental mapping of 30 nm large Fe(sal$_2$trien)⊂MOF-808 nanocrystals.

1⊂MOF-808 was further characterized using pair distribution function (PDF) that gives access to the interatomic distances in amorphous or crystalline solids. The differential signal between **1**⊂MOF-808 and MOF-808 presents characteristic peaks of the $Fe^{III}(sal_2trien)^+$ cation, suggesting that the coordination sphere of the complex is retained after loading (see **Fig. S6**). The Infrared and Raman spectra of all **1**⊂MOF-808 samples, including those of different MOF particle sizes and complex loading amounts, match well the characteristic peaks from **1,** further confirming the successful complex encapsulation (**Fig. 2 and Fig. S7**). The most intense peaks of MOF-808 (at 1000 cm^{-1} and 1450 cm^{-1}) are also distinguished in the infrared spectra of the hybrid composites.

The amount of complexes loaded in MOF-808 was then tuned by adjusting the concentration of the SCO solution used for the loading process. By decreasing the starting ratio of **1**:MOF-808 from 1:2 to 1:12, the incorporated amount of loaded complex proportionately decreased by a factor of 4 and the Fe : Zr ratio reached 0.055. The MOF-808 particle size therefore has a negligible impact on the loading capacity. In details, the largest particle size (850 nm) has the highest Fe loading with an Fe/Zr ratio of 0.3, which corresponds to approximately 7.2 SCO molecules *per* cage, while the 30 nm particles contain 6.8 SCO molecules *per* cage.

1⊂MOF-808	MOF-808 particle size	Mass ratio of reactants, $m_{MOF} : m_1$	Average Fe : Zr atomic ratio by EDX	Molecules per cage
1⊂120 nm-21%	120 nm	2 : 1	0.21 ± 0.03	5.1 SCO/cage
1⊂120 nm-8%	120 nm	6 : 1	0.08 ± 0.01	1.9 SCO/cage
1⊂120 nm-5.5%	120 nm	12 : 1	0.055 ± 0.01	1.2 SCO/cage
1⊂30 nm	30 nm	2 : 1	0.28 ± 0.04	6.8 SCO/cage
1⊂850 nm	850 nm	2 : 1	0.30± 0.04	7.2 SCO/cage

Table 1. Summary of all 1⊂MOF-808 composites with different particle sizes and various synthetic conditions.

The porosity of MOF-808 and **1**⊂MOF-808 composites was evaluated by N_2 porosimetry (at 77K). The parent MOF-808 compounds showed comparable Brunauer–Emmett–Teller (BET) surface areas (2080 m^2/g) and nitrogen uptakes (480 cm^3/g) to those reported before.[25,26] After incorporating the Fe complex, both nitrogen uptake and BET surface area decreased, which is consistent with Fe(sal_2trien)NO_3 molecules occupying the pores of the host matrix (**Fig. 2 and Fig. S8-9**). Noticeably, the pore size distribution (see **Fig. S8-9** for details) indicates that the compounds maintained a residual microporosity from the tetrahedral cages, even for the maximum loading, with the porosity associated to the 18.4 Å adamantane cages being reduced significantly, corroborating the successful loading of the Fe complex into these large pores.

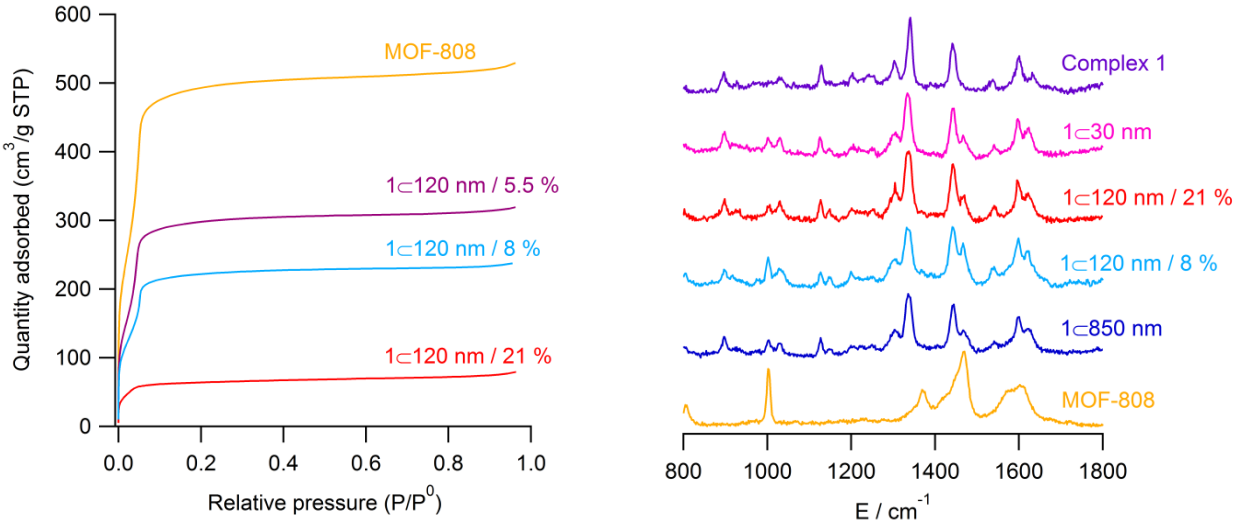

Figure 2. (left) N_2 sorption isotherms at 77 K (P_0=1 bar) of 120 nm MOF-808 nanocrystals with different iron complex loading; (right) Raman spectra of MOF-808 nanocrystals ($\lambda_{excitation}$ = 785 nm) with different particle sizes and iron complex loadings.

- **$Fe^{III}(sal_2trien)$⊂MOF-808 thermal switching**

Variable temperature magnetic susceptibility measurements were then performed on **1**⊂MOF-808 samples at a sweep rate of 0.5 K/min in order to study their switching behavior (see Supporting information for the data processing). While $Fe(sal_2trien)NO_3$ stayed in the LS state at all temperatures,[30] all composites with a saturated loadings showed an abrupt thermal transition centered around 281 K (280.1 K for 850 nm host, 284.0 K for 120 nm, 280.6 K for 30 nm). Noticeably, the transition did not proceed to completeness for all three samples. At 150K, $\chi_M T$ values are 1.6 emu·K·mol^{-1} for 850 nm, 1.25 emu·K·mol^{-1} for 120 nm and 1.8 emu·K·mol^{-1} for 30 nm MOF particle size corresponding to approximately 70%, 78%, and 65% of LS Fe^{III}, respectively. At 400K, χ_MT showed a value of 3.24 emu·K·mol^{-1} for 850 nm MOF-808 particles, which indicates that ca. 25% of Fe^{III} remains LS. A similar residual LS fraction at high temperature was observed for 120 and 30 nm nanoparticles. Therefore, regardless of the MOF particle size, ca. 50% of the Fe^{III} complexes undergo a thermal spin crossover. Moreover, 20 to 30 K wide thermal hysteresis loops were observed irrespective of the particle size. In the literature, size reduction often leads to a decrease in transition temperature and loss of cooperativity.[10,11] Notably, such deterioration is not present in the **1**⊂MOF-808 system that present an abrupt thermal transition with the opening of an hysteresis loop close to room temperature regardless of crystal size. This suggests that the bistability observed in **1**⊂MOF-808 originates from short-range interactions between the SCO complex and the MOF backbone inside the adamantane cage rather than from long-range interactions occurring in the whole solid.

To further investigate the switching behavior of the **1**⊂MOF-808 composites, measurements were performed at different sweep rates from 2 K/min to 0.25 K/min on the 120 nm sample. Decreasing the sweep rate led to a more complete thermal transition, revealing the slow kinetics of the thermal spin transition. This observation was somehow unexpected for Fe^{III} SCO solids that typically present much faster spin transition dynamics around room temperature[35] and again suggests the existence of strong host-guest interactions between the SCO complexes and the MOF backbone influencing the spin crossover kinetics.

We then explored the effect of the SCO loading on the thermal spin crossover behavior of **1**⊂MOF-808. Surprisingly, the compound with the lowest Fe loading (1⊂120 nm-5.5% (that contains approximately 1.2 complexes per cage), still displayed a thermally induced spin transition located at 280.3 K with a 24.2 K wide hysteresis loop, comparable to the sample containing 6 complexes per cage (see **Fig. S10**). Furthermore, a lower residual Fe^{III} HS fraction was observed at 150 K compared to a higher loading sample (χ_MT of 1.30 emu·K·mol^{-1} at 200 K *vs*. 1.49 emu·K·mol^{-1} for the highest loading). Keeping a wide thermal hysteresis at low complex loading strongly supports the presence of strong interactions between the MOF backbone and the SCO complex. Indeed, lowering the concentration of the Fe^{III} complex in a host matrix usually leads to a gradual spin transition, as it weakens the intermolecular interactions at the origin of cooperative processes.[36]

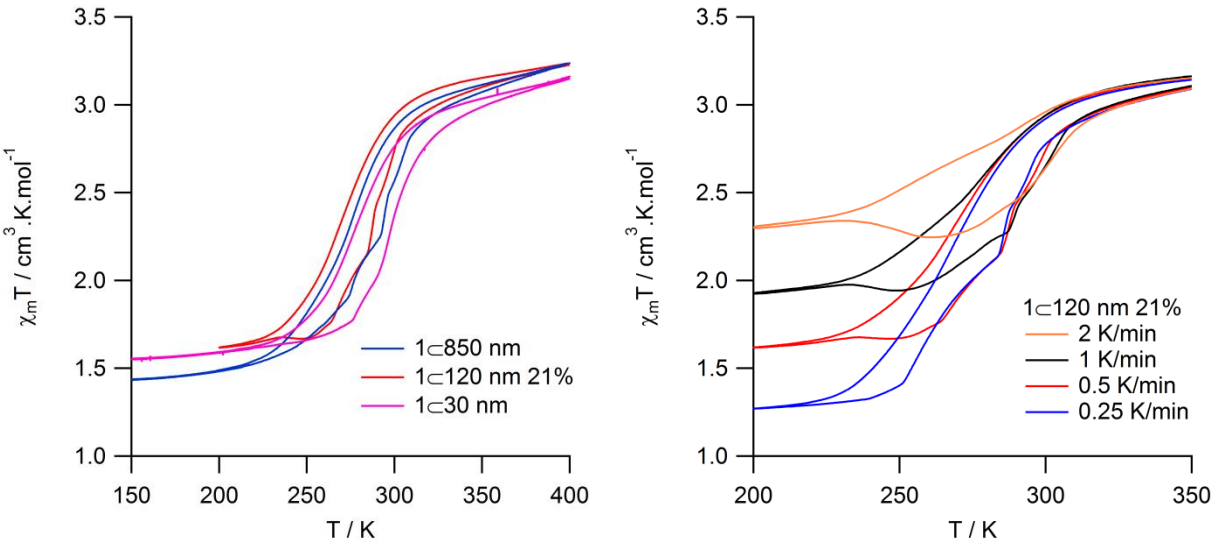

Figure 3. Evolution of the product of the molar magnetic susceptibility multiplied by the temperature (left) as function of the temperature measured at 0.5 K/min for different MOF particle sizes and (right) as function of the sweep rate for a given sample.

Variable temperature Mössbauer spectra were then registered on a 1⊂120 nm, a powdered sample enriched in ^{57}Fe (see **Fig. 4**). At 300 and 77 K, the spectra can be well described with two asymmetrical quadrupolar doublets, attributed to LS and HS $Fe^{III}(sal_2trien)^+$ species and the presence of some preferential effect (see Supporting Information for the fitting details). Cooling down the sample led to a decrease in the HS fraction from γ_{HS} = 0.77 at 300 K to γ_{HS} = 0.49 at 77 K, in agreement with magnetic susceptibility measurements. Notably, the HS species showed a slightly higher quadrupolar splitting (0.73 mm.s^{-1} at 300 K) than those reported for $Fe^{III}(sal_2trien)^+$ in molecular crystals or loaded in oxalate networks (ranging from 0 to 0.5 mm.s^{-1}).[30,37–39] This suggests a slightly more distorted environment around HS Fe^{III} ions once loaded in MOF-808 than in the reference compounds, which may be due to strong host-guest interactions between the $Fe^{III}(sal_2trien)^+$ species and the MOF backbone. On the opposite, the LS species presented both an isomer shift and a quadrupolar splitting perfectly in line with the reported values.

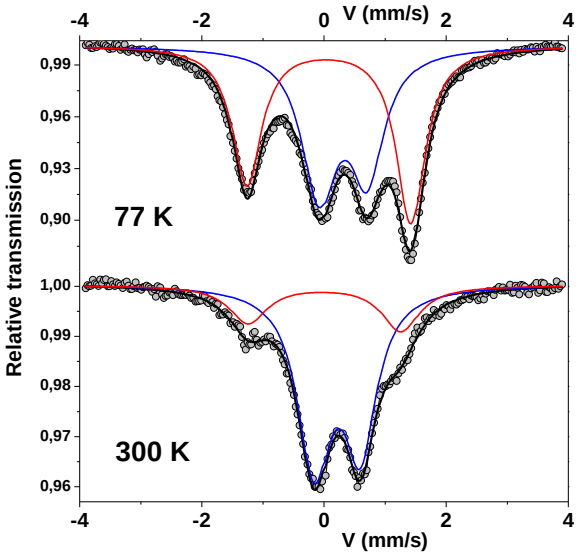

Figure 4. Mössbauer spectra of ^{57}Fe enriched 1⊂120nm-21% at 300 K and 77 K. The HS and LS components are in blue and red, respectively.

- **Modeling of the host-guest interactions**

In order to decipher the interactions between **1** and MOF-808 at the origin of the experimental observations, the preferential locations of the complex in the MOF have been determined by combining well-tempered metadynamics (WT-MTD) simulations[40] performed with the tight-binding GFN-xTB method[41] and structural optimizations carried out within DFT.[42,43] At first, the WT-MTD were applied to determine the most favorable locations of $Ga^{III}(sal_2trien)^+$ (**2**) in MOF-808 in presence of the NO_3^- as counter-ion. The choice of the model system **2**⊂MOF-808 is motivated by the facts (i) that Ga(III) and HS Fe(III) have similar ionic radii and (ii) that this system being a closed-shell system, the simulations done in a spin-restricted framework are computationally far less demanding than those that would be required for the open-shell **1**⊂MOF-808 system. For our purposes, the relevant collective variables (CVs) used for sampling the free energy surface (FES) of **2**⊂MOF-808 are the Cartesian coordinates of the Ga atoms (see SI for the Computational details). **Fig. 5** shows the reconstructed FES $F(T; x_{Ga}, y_{Ga}, z_{Ga})$ (simulations performed at T = 350 K), evidencing that **2** are preferentially located close to the walls of the cavities of the MOF-808.

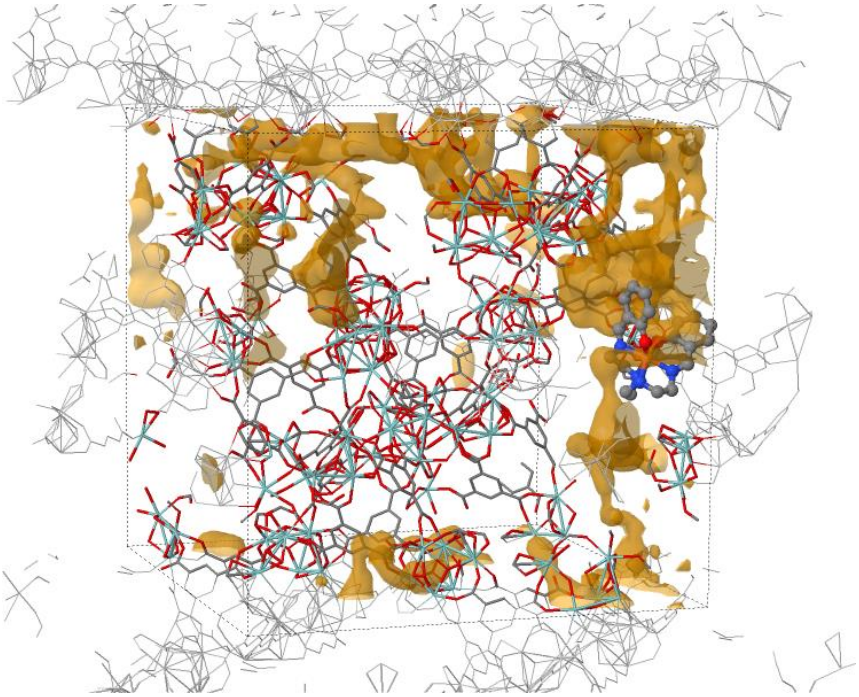

Figure 5. Reconstructed FES $F(T; x_{Ga}, y_{Ga}, z_{Ga})$ of **2**⊂MOF-808 obtained from the WT-MTD simulations performed at T = 350 K (F = -50 mHa) superimposed with the optimized HS structure of **1**⊂MOF-808 obtained from the configuration 2 (see Text).

The FES exhibits a myriad of minima (179 could be located) and the four most stable minima have been retained for further analysis. Table S2 lists the coordinates (x_{Ga}, y_{Ga}, z_{Ga}) of the Ga(III) ion and the values of free energy at these minima, as well as the corresponding snapshots. The most stable minimum of the FES results from the decomplexation of **2** and the migration of the Ga(III) ion into the MOF-808 host. For the three other minima, the complex is preserved and anchored to the wall of the host owing to π-π interactions involving a phenoxy ring of the ligand of the complex and a phenyl ring of the MOF. After having replaced Ga(III) by Fe(III), these three snapshots were used as starting points to optimize the structures of **1**⊂MOF-808 in the LS and HS states using the dispersion corrected PBE-D3 functional (see **Fig. 6** and the SI for the Computational details).

Table 2: Selected bond lengths (Å) and angular parameters (°) characterizing the geometry of $Fe^{III}(sal_2trien)^+$ in the DFT-optimized LS and HS geometries of **1**⊂MOF-808 for the considered configurations. The values found for these structural parameters in the optimized gas-phase LS and HS geometries of the complex are also given.

	Configuration 1		Configuration 2		Configuration 3		Gas phase	
	LS	HS	LS	HS	LS	HS	LS	HS
Fe-O_1	1.888	1.937	1.884	1.938	1.880	1.982	1.847	1.919
Fe-O_1'	1.889	1.967	1.871	1.928	1.867	1.938	1.861	1.907

Fe-N_1	1.910	2.097	1.923	2.121	1.927	2.107	1.918	2.109
Fe-N_2	2.080	2.292	2.040	2.231	2.021	2.216	2.035	2.251
Fe-N_1'	2.039	2.198	2.079	2.274	2.047	2.229	2.050	2.243
Fe-N_2'	1.975	2.104	1.968	2.124	1.941	2.128	1.936	2.078
Σ	92.2	120.8	61.0	92.8	61.2	111.7	45.3	71.5
Θ	306.0	502.4	172.9	306.4	169.5	378.9	117.4	188.5
α	86.7	88.0	64.9	61.1	67.9	67.8	66.9	64.9

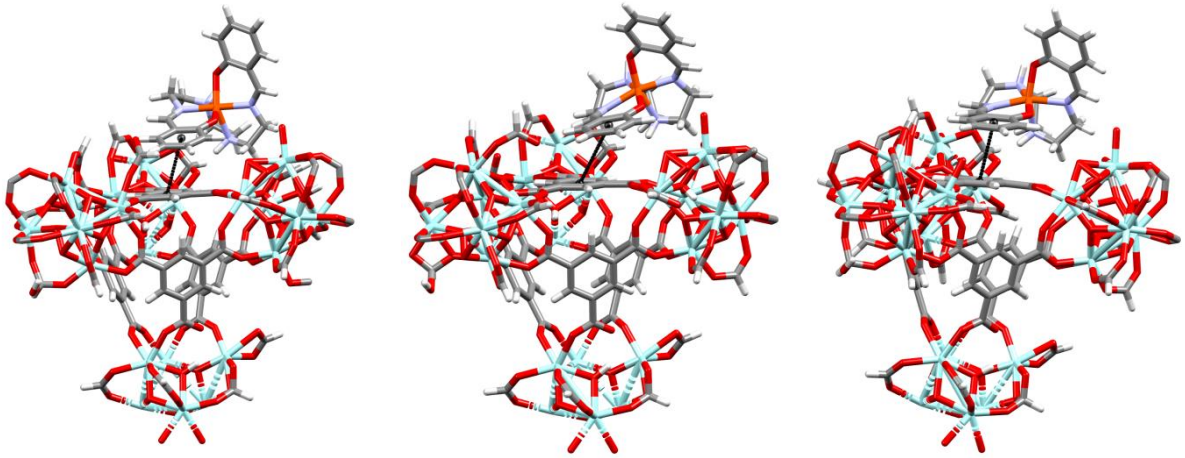

Figure 6. Snapshots of the structures of the three most stable minima of **1**⊂MOF-808 located on the estimate of the FES and further optimized by DFT, the shortest contacts between the MOF-808 linker and the SCO complex are evidenced by the black line.

Table 2 summarizes the values of the structural parameters selected for characterizing the structure of $Fe^{III}(sal_2trien)^+$ in the DFT-optimized LS and HS geometries of **1**⊂MOF-808: the Fe-O and Fe-N bond lengths, the parameter Σ that measures the deviation of the complex from an octahedral structure, the parameter Θ that measures the distortion from a perfect octahedral (O_h) towards a trigonal prismatic (D_{3h}) geometry and α, the dihedral angle between the least squares planes of the two phenoxy rings of the $Fe^{III}(sal_2trien)^+$ linker (see ESI for the definition of these parameters). For the encaged and the isolated complexes in either spin state, the Fe-O and Fe-N bond lengths are consistent with those determined by single crystal X-Ray diffraction on $Fe^{III}(sal_2trien)^+$ based compounds.[27] Concerning the distortion from the octahedral geometry, Halcrow *et al.* found that Σ =40-47° and Θ =56-98° in the LS structures and that Σ =86-118° and Θ =204-358° in the HS structures, which reflects larger and variable deviations from an ideal octahedral structure in the HS state than in the LS state.[27] The calculated values of Σ and Θ for $Fe^{III}(sal_2trien)^+$ in the gas-phase correspond to or are below the lower bound of the reported experimental values. However, they drastically increase on passing to the geometries of $Fe^{III}(sal_2trien)^+$ in **1**⊂MOF-808, which means that $Fe^{III}(sal_2trien)^+$ complexes are more distorted when loaded in MOF-808 due to the strong host-guest

interactions. In particular, the HS configurations are much more distorted than in the gas phase and in all the reported experimental structures. This qualitatively agrees with the Mössbauer results that suggest a highly distorted HS geometry of the $Fe^{III}(sal_2trien)^+$ cations when loaded into MOF-808. In addition, the anchoring of the complex can take place in different manners, leading to complexes exhibiting various degrees of deviation from an ideal octahedral geometry, which may explain the broadening of the Mössbauer lines. The angle α takes values lower than 90°, which experimentally correspond to LS and spin crossover complexes, while α > 90° tends to be observed for HS or mixed-spin molecules that do no present spin crossover.[27] Therefore, the values of α in the characterized configurations of the studied **1**⊂MOF-808 are consistent with the fact that this compound undergoes a thermal spin crossover.

In summary, the computational study evidenced that the anchoring of $Fe^{III}(sal_2trien)^+$ to the MOF-808 host proceeds mainly through π-π interactions. The complexes present a distorted geometry when loaded in the MOF, yet compatible with a thermal spin crossover. These two observations strongly support the fact that the MOF-complex supramolecular interactions are the key point to explain the switching properties of **1**⊂MOF-808, as suggested by the magnetic measurements. More precisely, one can imagine that the interaction between $Fe^{III}(sal_2trien)^+$ and the MOF-808 structure forces the complex to stay in a distorted environment, which may add an additional energy barrier associated to the spin crossover process, giving rise to the appearance of an hysteresis loop in the thermal spin crossover. It is worth mentioning that the opening of the thermal hysteresis loop observed here is likely to be due to a localized host-guest interaction coupled to slow switching kinetics rather than a phase transition, as commonly observed in other spin crossover compounds. A detailed study of this switching mechanism is underway. Compared to what happens in molecular solids, this strategy can give rise to bistable compounds without interactions between neighboring SCO complexes, therefore allowing access to robust bistable nano-objects that are particularly appealing for the design of optical or sensing devices.

Conclusion

We have developed a method that for the first time leads to porous solids presenting an abrupt thermal spin transition with a large hysteresis loop close to room temperature, based on the encapsulation of Fe(III) spin crossover complexes in the pores of MOF-808, with a minimal dependence on the SCO loading capacity. This unexpected behavior can be explained by the strong host-guest interactions occurring in between the complex and the MOF scaffold, which creates an additional energy barrier affecting the spin transition behavior. The bistability observed here therefore comes from a molecular origin and hence does not depend on the MOF particle size or on the SCO loading capacity. This strategy opens broad perspectives for the design of bistable materials for display or sensing devices, as the switching properties are much more robust in this compound than in conventional spin crossover compounds where the cooperativity relies on elastic interactions.

Acknowledgments

AT thanks the ANR MOFSCO (ANR-18-CE09-0005-01) for funding. YS thanks the UptoParis European Union's Horizon 2020 research and innovation program under the Marie Skłodowska-Curie grant agreement No 754387. AT and YS thank F. Tournilhac (ESCPI, Paris) for his help on the Raman spectra data collection. AT thanks the Sesame project from the Ile-de-France region for the magnetometer and B. Leridon (ESPCI, Paris) for her help in the magnetization data collection. We thank Erik Elkaim from CRISTAL beamline (SOLEIL) for the help in collection of the synchrotron PDF data (proposal 20191257). LMLD acknowledges grants from the Swiss National Supercomputing Centre (CSCS) under project IDs s894 and s1072.

Supporting Information

Details of the synthetic protocols, additional characterization of the solids, methodology of the computational study.

References

(1) Bigdeli, F.; Lollar, C. T.; Morsali, A.; Zhou, H. Switching in Metal–Organic Frameworks. *Angew. Chem. Int. Ed.* **2020**, *59* (12), 4652–4669. https://doi.org/10.1002/anie.201900666.

(2) Li, H.-Y.; Zhao, S.-N.; Zang, S.-Q.; Li, J. Functional Metal–Organic Frameworks as Effective Sensors of Gases and Volatile Compounds. *Chem Soc Rev* **2020**, 38.

(3) Gütlich, P.; Gaspar, A. B.; Garcia, Y. Spin State Switching in Iron Coordination Compounds. *Beilstein J Org Chem* **2013**, 50.

(4) Spiering, H. Elastic Interaction in Spin Crossover Compounds. **2004**, 25. https://doi-org.inc.bib.cnrs.fr/10.1007/b95427.

(5) Molnar, G.; Mikolasek, M.; Ridier, K.; Fahs, A.; Nicolazzi, W.; Bousseksou, A. Molecular Spin Crossover Materials: Review of the Lattice Dynamical Properties. *Ann Phys* **2019**, 21.

(6) Halcrow, M. A. Structure:Function Relationships in Molecular Spin-Crossover Complexes. *Chem. Soc. Rev.* **2011**, *40* (7), 4119. https://doi.org/10.1039/c1cs15046d.

(7) Ohba, M.; Yoneda, K.; Agustí, G.; Muñoz, M. C.; Gaspar, A. B.; Real, J. A.; Yamasaki, M.; Ando, H.; Nakao, Y.; Sakaki, S.; Kitagawa, S. Bidirectional Chemo-Switching of Spin State in a Microporous Framework. *Angew. Chem. Int. Ed.* **2009**, *48* (26), 4767–4771. https://doi.org/10.1002/anie.200806039.

(8) Ni, Z.-P.; Liu, J.-L.; Hoque, Md. N.; Liu, W.; Li, J.-Y.; Chen, Y.-C.; Tong, M.-L. Recent Advances in Guest Effects on Spin-Crossover Behavior in Hofmann-Type Metal-Organic Frameworks. *Coord. Chem. Rev.* **2017**, *335*, 28–43. https://doi.org/10.1016/j.ccr.2016.12.002.

(9) Nakaya, M.; Ohtani, R.; Hayami, S. Guest Modulated Spin States of Metal Complex Assemblies. *Eur. J. Inorg. Chem.* **2020**, *2020* (39), 3709–3719. https://doi.org/10.1002/ejic.202000553.

(10) Volatron, F.; Catala, L.; Rivière, E.; Gloter, A.; Stéphan, O.; Mallah, T. Spin-Crossover Coordination Nanoparticles. *Inorg. Chem.* **2008**, *47* (15), 6584–6586. https://doi.org/10.1021/ic800803w.

(11) Molnár, G.; Rat, S.; Salmon, L.; Nicolazzi, W.; Bousseksou, A. Spin Crossover Nanomaterials: From Fundamental Concepts to Devices. *Adv. Mater.* **2018**, *30* (5), 1703862. https://doi.org/10.1002/adma.201703862.

(12) Raza, Y.; Volatron, F.; Moldovan, S.; Ersen, O.; Huc, V.; Martini, C.; Brisset, F.; Gloter, A.; Stéphan, O.; Bousseksou, A.; Catala, L.; Mallah, T. Matrix-Dependent Cooperativity in Spin Crossover Fe(Pyrazine)Pt(CN)4 Nanoparticles. *Chem. Commun.* **2011**, *47* (41), 11501. https://doi.org/10.1039/c1cc14463d.

(13) Tissot, A.; Enachescu, C.; Boillot, M.-L. Control of the Thermal Hysteresis of the Prototypal Spin-Transition FeII(Phen)2(NCS)2 Compound via the Microcrystallites Environment: Experiments and Mechanoelastic Model. *J. Mater. Chem.* **2012**, *22* (38), 20451. https://doi.org/10.1039/c2jm33865c.

(14) Enachescu, C.; Tanasa, R.; Stancu, A.; Tissot, A.; Laisney, J.; Boillot, M.-L. Matrix-Assisted Relaxation in $Fe(Phen)_2(NCS)_2$ Spin-Crossover Microparticles, Experimental and Theoretical Investigations. *Appl. Phys. Lett.* **2016**, *109* (3), 031908. https://doi.org/10.1063/1.4959262.

(15) Delgado, T.; Enachescu, C.; Tissot, A.; Guénée, L.; Hauser, A.; Besnard, C. The Influence of the Sample Dispersion on a Solid Surface in the Thermal Spin Transition of $[Fe(Pz)Pt(CN)_4]$ Nanoparticles. *Phys. Chem. Chem. Phys.* **2018**, *20* (18), 12493–12502. https://doi.org/10.1039/C8CP00775F.

(16) Umemura, Y.; Minai, Y.; Koga, N.; Tominaga, T. Spin-Crossover of Tris[2-(Aminomethyl)Pyridine]Iron(II) Ion in Y-Zeolite. *J. Chem. Soc. Chem. Commun.* **1994**, No. 7, 893. https://doi.org/10.1039/c39940000893.
(17) Field, C. N.; Boillot, M.-L.; Clément, R. Observation of a Thermally Induced Spin Crossover in a CdPS3 Intercalate. *J. Mater. Chem.* **1998**, *8* (2), 283. https://doi.org/10.1039/A707887K.
(18) Abhervé, A.; Grancha, T.; Ferrando-Soria, J.; Clemente-León, M.; Coronado, E.; Waerenborgh, J. C.; Lloret, F.; Pardo, E. Spin-Crossover Complex Encapsulation within a Magnetic Metal–Organic Framework. *Chem. Commun.* **2016**, *52* (46), 7360–7363. https://doi.org/10.1039/C6CC03667H.
(19) Zhao, T.; Boldog, I.; Spasojevic, V.; Rotaru, A.; Garcia, Y.; Janiak, C. Solvent-Triggered Relaxative Spin State Switching of [Fe(HB(Pz) $_3$) $_2$] in a Closed Nano-Confinement of NH $_2$ -MIL-101(Al). *J. Mater. Chem. C* **2016**, *4* (27), 6588–6601. https://doi.org/10.1039/C6TC01297C.
(20) Mínguez Espallargas, G.; Coronado, E. Magnetic Functionalities in MOFs: From the Framework to the Pore. *Chem. Soc. Rev.* **2018**, *47* (2), 533–557. https://doi.org/10.1039/C7CS00653E.
(21) Furukawa, H.; Cordova, K. E.; O'Keeffe, M.; Yaghi, O. M. The Chemistry and Applications of Metal-Organic Frameworks. *Science* **2013**, *341* (6149), 1230444. https://doi.org/10.1126/science.1230444.
(22) Tissot, A.; Kesse, X.; Giannopoulou, S.; Stenger, I.; Binet, L.; Rivière, E.; Serre, C. A Spin Crossover Porous Hybrid Architecture for Potential Sensing Applications. *Chem. Commun.* **2018**, *55* (2), 194–197. https://doi.org/10.1039/C8CC07573E.
(23) Moreau, F.; Marrot, J.; Banse, F.; Serre, C.; Tissot, A. Sequential Installation of Fe(Ii) Complexes in MOFs: Towards the Design of Solvatochromic Porous Solids. *J. Mater. Chem. C* **2020**, *8* (47), 16826–16833. https://doi.org/10.1039/D0TC03756G.
(24) Zhao, T.; Dong, M.; Zhao, Y. A Novel Fabrication of [Fe(HB(Pz)3)2]@MIL-101 Hybrid Material via Diffusion and the Lower Temperature Shift on Its Spin Transition Behavior. *Appl. Phys. A* **2019**, *125* (9), 670. https://doi.org/10.1007/s00339-019-2970-5.
(25) Furukawa, H.; Gándara, F.; Zhang, Y.-B.; Jiang, J.; Queen, W. L.; Hudson, M. R.; Yaghi, O. M. Water Adsorption in Porous Metal–Organic Frameworks and Related Materials. *J. Am. Chem. Soc.* **2014**, *136* (11), 4369–4381. https://doi.org/10.1021/ja500330a.
(26) Dai, S.; Simms, C.; Dovgaliuk, I.; Patriarche, G.; Tissot, A.; Parac-Vogt, T. N.; Serre, C. Monodispersed MOF-808 Nanocrystals Synthesized via a Scalable Room-Temperature Approach for Efficient Heterogeneous Peptide Bond Hydrolysis. *Chem. Mater.* **2021**, acs.chemmater.1c02174. https://doi.org/10.1021/acs.chemmater.1c02174.
(27) Pritchard, R.; Barrett, S. A.; Kilner, C. A.; Halcrow, M. A. The Influence of Ligand Conformation on the Thermal Spin Transitions in Iron(Iii) Saltrien Complexes. *Dalton Trans.* **2008**, No. 24, 3159. https://doi.org/10.1039/b801892h.
(28) Juhás, P.; Davis, T.; Farrow, C. L.; Billinge, S. J. L. PDFgetX3: A Rapid and Highly Automatable Program for Processing Powder Diffraction Data into Total Scattering Pair Distribution Functions. *J. Appl. Crystallogr.* **2013**, *46* (2), 560–566. https://doi.org/10.1107/S0021889813005190.
(29) Farrow, C. L.; Juhas, P.; Liu, J. W.; Bryndin, D.; Božin, E. S.; Bloch, J.; Proffen, T.; Billinge, S. J. L. PDFfit2 and PDFgui: Computer Programs for Studying Nanostructure in Crystals. *J. Phys. Condens. Matter* **2007**, *19* (33), 335219. https://doi.org/10.1088/0953-8984/19/33/335219.
(30) Sinn, E.; Sim, G.; Dose, E. V.; Tweedle, M. F.; Wilson, L. J. Iron(III) Chelates with Hexadentate Ligands from Triethylenetetramine and .Beta.-Diketones or Salicylaldehyde. Spin State Dependent Crystal and Molecular Structures of [Fe(Acac)2trien]PF6(S = 5/2), [Fe(AcacCl)2trien]PF6(S = 5/2), [Fe(Sal)2trien]Cl.2H2O(S = 1/2), and [Fe(Sal)2trien]NO3.H2O(S = 1/2). *J. Am. Chem. Soc.* **1978**, *100* (11), 3375–3390. https://doi.org/10.1021/ja00479a021.
(31) Greneche, J. M.; Varret, F. On the Texture Problem in Mossbauer Spectroscopy. *J. Phys. C Solid State Phys.* **1982**, *15*, 5333–5344.
(32) Greneche, J.M.; Varret, F. A New Method of General Use to Obtain Random Powder Spectra in 57Fe Mössbauer Spectroscopy : The Rotating-Sample Recording. *J Phys. Lett* **1982**, *43* (7), 233–237. https://doi.org/10.1051/jphyslet:01982004307023300.
(33) Wang, S.; Ly, H. G. T.; Wahiduzzaman, M.; Simms, C.; Dovgaliuk, I.; Tissot, A.; Maurin, G.; Parac-Vogt, T. N.; Serre, C. A Zirconium Metal-Organic Framework with SOC Topological Net for Catalytic Peptide Bond Hydrolysis. *Nat. Commun.* **2022**, *13* (1), 1284. https://doi.org/10.1038/s41467-022-28886-5.
(34) Canioni, R.; Roch-Marchal, C.; Sécheresse, F.; Horcajada, P.; Serre, C.; Hardi-Dan, M.; Férey, G.; Grenèche, J.-M.; Lefebvre, F.; Chang, J.-S.; Hwang, Y.-K.; Lebedev, O.; Turner, S.; Van Tendeloo, G. Stable Polyoxometalate Insertion within the Mesoporous Metal Organic Framework MIL-100(Fe). *J Mater Chem* **2011**, *21* (4), 1226–1233. https://doi.org/10.1039/C0JM02381G.

(35) Hauser, A. Light-Induced Spin Crossover and the High-Spin→Low-Spin Relaxation. In *Spin Crossover in Transition Metal Compounds II*; Topics in Current Chemistry; Springer Berlin Heidelberg: Berlin, Heidelberg, 2004; Vol. 234, pp 155–198. https://doi.org/10.1007/b95416.
(36) Haddad, M. S.; Federer, W. D.; Lynch, M. W.; Hendrickson, D. N. Spin-Crossover Ferric Complexes: Unusual Effects of Grinding and Doping Solids. *Inorg. Chem.* **1981**, *20* (1), 131–139. https://doi.org/10.1021/ic50215a029.
(37) Clemente-León, M.; Coronado, E.; Giménez-López, M. C.; Soriano-Portillo, A.; Waerenborgh, J. C.; Delgado, F. S.; Ruiz-Pérez, C. Insertion of a Spin Crossover Fe ^{III} Complex into an Oxalate-Based Layered Material: Coexistence of Spin Canting and Spin Crossover in a Hybrid Magnet. *Inorg. Chem.* **2008**, *47* (19), 9111–9120. https://doi.org/10.1021/ic801165b.
(38) Clemente-León, M.; Coronado, E.; López-Jordà, M.; Waerenborgh, J. C.; Desplanches, C.; Wang, H.; Létard, J.-F.; Hauser, A.; Tissot, A. Stimuli Responsive Hybrid Magnets: Tuning the Photoinduced Spin-Crossover in Fe(III) Complexes Inserted into Layered Magnets. *J. Am. Chem. Soc.* **2013**, *135* (23), 8655–8667. https://doi.org/10.1021/ja402674x.
(39) Vieira, B. J. C.; Coutinho, J. T.; Santos, I. C.; Pereira, L. C. J.; Waerenborgh, J. C.; da Gama, V. [Fe(Nsal$_2$ Trien)]SCN, a New Two-Step Iron(III) Spin Crossover Compound, with Symmetry Breaking Spin-State Transition and an Intermediate Ordered State. *Inorg. Chem.* **2013**, *52* (7), 3845–3850. https://doi.org/10.1021/ic302533b.
(40) Barducci, A.; Bussi, G.; Parrinello, M. Well-Tempered Metadynamics: A Smoothly Converging and Tunable Free-Energy Method. *Phys Rev Lett* **2008**, *100* (2), 020603. https://doi.org/10.1103/PhysRevLett.100.020603.
(41) Grimme, S.; Bannwarth, C.; Shushkov, P. A Robust and Accurate Tight-Binding Quantum Chemical Method for Structures, Vibrational Frequencies, and Noncovalent Interactions of Large Molecular Systems Parametrized for All Spd-Block Elements (Z = 1–86). *J. Chem. Theory Comput.* **2017**, *13* (5), 1989–2009. https://doi.org/10.1021/acs.jctc.7b00118.
(42) Hohenberg, P.; Kohn, W. Inhomogeneous Electron Gas. *Phys Rev* **1964**, *136* (3B), B864–B871. https://doi.org/10.1103/PhysRev.136.B864.
(43) Kohn, W.; Sham, L. J. Self-Consistent Equations Including Exchange and Correlation Effects. *Phys Rev* **1965**, *140* (4A), A1133–A1138. https://doi.org/10.1103/PhysRev.140.A1133.

Table of contents